




Vectorial birefringence imaging by optical coherence microscopy for assessing fibrillar microstructures in the cornea and limbus

QINGYUN LI,^{1,*} KAROL KARNOWSKI,^{1,2}  GAVRIELLE UNTRACHT,¹  PETER B. NOBLE,³ BARRY CENSE,¹ MARTIN VILLIGER,^{4,6}  AND DAVID D. SAMPSON^{1,5,6}

¹Optical+Biomedical Engineering Laboratory, Department of Electrical, Electronic & Computer Engineering, The University of Western Australia, Perth, WA 6009, Australia

²Institute of Physical Chemistry, Polish Academy of Sciences, Kasprzaka 44/52, 01-224 Warsaw, Poland

³School of Human Sciences, The University of Western Australia, Perth, WA 6009, Australia

⁴Wellman Center for Photomedicine, Harvard Medical School and Massachusetts General Hospital, Boston, MA 02114, USA

⁵Surrey Biophotonics, School of Physics and School of Biosciences and Medicine, University of Surrey, Guildford, Surrey GU2 7XH, United Kingdom

⁶These authors share senior authorship equally

*21800152@student.uwa.edu.au

Abstract: The organization of fibrillar tissue on the micrometer scale carries direct implications for health and disease but remains difficult to assess *in vivo*. Polarization-sensitive optical coherence tomography measures birefringence, which relates to the microscopic arrangement of fibrillar tissue components. Here, we demonstrate a critical improvement in leveraging this contrast mechanism by employing the improved spatial resolution of focus-extended optical coherence microscopy (1.4 μm axially in air and 1.6 μm laterally, over more than 70 μm depth of field). Vectorial birefringence imaging of sheep cornea *ex vivo* reveals its lamellar organization into thin sections with distinct local optic axis orientations, paving the way to resolving similar features *in vivo*.

© 2020 Optical Society of America under the terms of the [OSA Open Access Publishing Agreement](#)

1. Introduction

Fibrillar collagen is the main structural extracellular matrix protein in mammals and an essential component of connective tissues. The microscopic organization of collagen fibers directly impacts the mechanical and structural tissue properties. There remains a strong need to assess this microscopic tissue organization, which is critical for physiological function, without involving biopsies of delicate tissues, non-invasively, and compatible with a clinical setting. One prominent example of need is the arrangement of collagen fibers in the cornea, which provides both mechanical protection of the eye and the optical transparency required for visual acuity [1]. High-resolution microscopy, including scanning electron microscopy [2,3] and X-ray scattering [4,5] of histological sample preparations, has been used to study collagen morphology in the cornea in great detail. The microscopic tissue organization of unstained sections is also accessible to polarized light microscopy (PLM) [6–8] and nonlinear microscopy [9–11]. Although second harmonic generation (SHG) is more efficient in transmission, it can be performed *in vivo* in reflection, as demonstrated in rats [11]. Yet, its low scattering cross section, need for high numerical aperture, resulting small field of view and long acquisition times complicate practical imaging in patients. In comparison, Brillouin microscopy has been successfully demonstrated *in vivo* in humans [12], albeit at modest imaging speed. Rather than directly visualizing tissue microstructure, it probes the mechanical properties of the sample through measurements of the local longitudinal elastic modulus [13,14].

Optical coherence tomography (OCT) reveals the subsurface microstructure of biological tissue by measuring the pathlength of backscattered light and is routinely used for imaging the geometry of the anterior eye in humans, owing to its high imaging speed and reflection geometry [15,16]. With the improved spatial resolution of optical coherence microscopy (OCM), many details of the weakly scattering structures in the cornea emerge [17–20]. However, because the backscattering signal amplitude does not directly depend on the orientation of individual collagen fibers, OCM lacks the specificity needed to identify differently oriented fibers and reveal their detailed organization.

Collagen and other fibrillar tissues, such as muscle and nerves, exhibit birefringence, whereby light polarized along the fibrils' axis experiences a delay relative to light polarized orthogonally. Birefringence serves as the contrast mechanism underlying PLM [21,22] and polarization-sensitive (PS-) OCT [23,24]. PLM measures the modification of known input polarization states upon transmission through physically sliced, thin histological sections to determine the amount of retardance as well as its vectorial property, the optic axis (OA) orientation, *i.e.*, the angle of linear polarization experiencing the smallest delay through the sample. PS-OCT, in comparison, uses coherence gating to measure the depth-resolved cumulative polarization effect of round-trip propagation to a given pathlength, without physically cutting any tissue. Recently developed processing strategies enable the elucidation of the polarization states of light backscattered within tissue; the reconstruction of depth-resolved birefringence and OA orientation from these cumulative measurements [25–28]. They isolate the polarization properties of a given depth location from the effect of preceding tissue layers to leverage the physical (in-plane) orientation of fibrillar structures as a compelling contrast mechanism. Yet, to date, the spatial resolution of the employed PS-OCT systems has been insufficient to resolve intricate features of fibrillar structures on the micrometer scale.

Here, we combine the high spatial resolution of OCM with local OA imaging to complement the detailed backscattering tomograms of the subsurface microstructure to give valuable insight into the organization and orientation of fibrillar tissue components. Our focus-extended PS-OCM system provides close to isotropic resolution $< 2 \mu\text{m}$. It employs a Bessel-like beam for illumination and a decoupled Gaussian detection mode to maintain high lateral resolution over an extended depth of field (DOF) and preserves the parallel depth imaging capability of OCT [29,30]. The polarization state of the light illuminating the sample is modulated between A-lines and two spectrometers detect orthogonal polarization states to measure the full Jones matrix. We adapted our recently developed correction and reconstruction method to extract the relative OA orientation with high axial resolution [28]. Focus-extended PS-OCM of sheep limbus and cornea, imaged *ex vivo*, demonstrates the unique capability of local OA imaging with improved spatial resolution by revealing the organization of the collagen fibers in these tissues into thin, stacked lamellae with distinct in-plane orientations. If operated at contemporary imaging speed, focus-extended PS-OCM could serve to investigate these microscopic tissue features in human corneas and other tissues *in vivo*.

2. Materials and methods

2.1. Focus-extended PS-OCM

The system was designed to define an extended DOF by illuminating the sample with a Bessel-like beam and using a decoupled Gaussian detection mode [31]. It employed two spectrometers for polarization-diverse detection and inter-A-line modulation of the illumination polarization state for polarization-sensitive imaging. As depicted in Fig. 1, unpolarized light from a supercontinuum source (SuperK Extreme EXR-1, NKT Photonics, Denmark) with a 3 dB bandwidth exceeding 200 nm centered on 800 nm was split into reference (10%) and sample arms (90%) by a wideband fiber coupler (TW805R2A2, Thorlabs Inc., New Jersey, USA). A polarization modulation unit, consisting of a linear polarizer (FBR-LPNIR, Thorlabs Inc.) and an electro-optic modulator

(EOM, 4102NF, Newport Corp., California, USA), modulated the input polarization state, A-line by A-line, between right- and left-handed circularly polarized light [32,33]. The polarizer filtered the unpolarized source light to a linear state oriented at 45° to the optic axis of the EOM, which was driven to operate as a quarter-waveplate (for the central wavelength) with alternating positive and negative retardation. The polarization-modulated light is coupled back into a single-mode fiber and no attempt was made to control the polarization states incident on the sample.

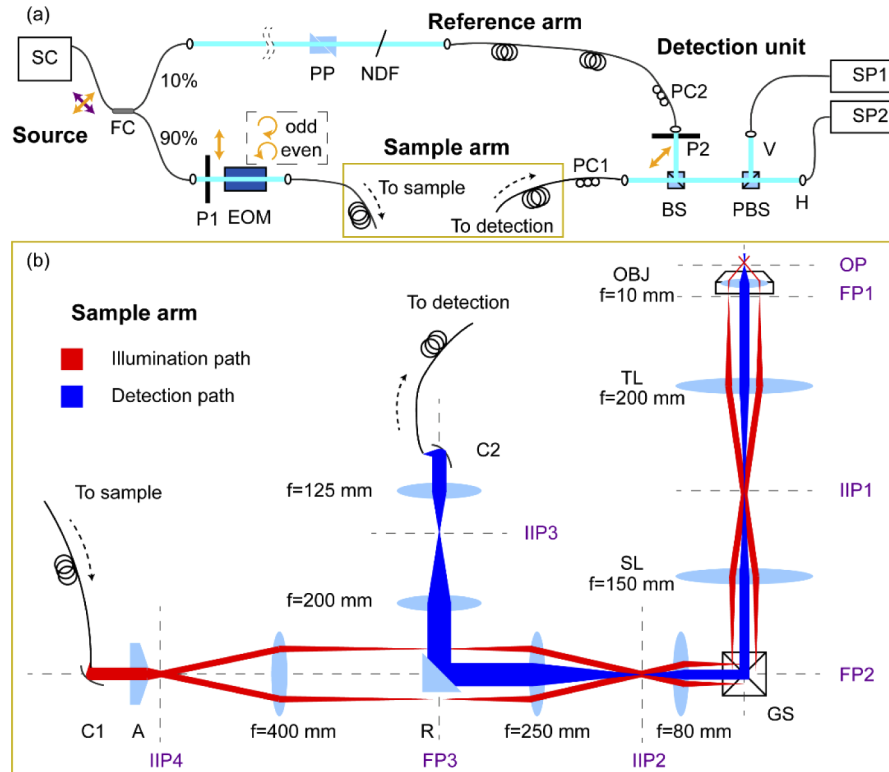


Fig. 1. System schematic. (a) The main body of the interferometer. Single-mode fibers are used throughout the system. Thick and solid cyan lines indicate free-space propagation. SC, supercontinuum; FC, fiber coupler; P, polarizer; EOM, electro-optic modulator; PP, prism pair; NDF, neutral density filter; PC, polarization controller; BS, beam splitter; PBS, polarizing beam splitter; R, reflector; SP, spectrometer. Only one coherent component of the light from the source (indicated by the orange arrows throughout) is used for imaging; whereas, the incoherent component, *i.e.*, the orthogonally polarized light (indicated by the purple arrow), is filtered out in the sample arm and in the reference arm by the polarizers P1 and P2, respectively. The EOM modulates between A-lines the polarization state of the light passing through, such that the light of odd and even A-lines is right and left circularly polarized (for the central wavelength), respectively. (b) The setup of the sample arm. C, collimator; A, axicon; GS, galvanometric scanner; SL, scan lens; TL, tube lens; OBJ, objective; OP, object plane; FP, Fourier plane; IIP, intermediate image plane.

In the illumination path of the sample arm, collimated light from a reflective collimator (RC02APC-P01, Thorlabs Inc.) impinged on the flat surface of a 176° -apex angle axicon lens (XFL25-020-U-B, Asphericon GmbH, Jena, Germany) to create a Bessel-like beam with a Fresnel number of 10.9, which offered a good trade-off between DOF extension and SNR penalty [34]. An achromatic doublet lens with 400 mm focal length (AC254-400-B, Thorlabs Inc.) transformed the Bessel beam into a thin annulus (11 mm in diameter), accommodating a 6 mm-diameter,

45° rod mirror (#49-399, Edmund Optics, New Jersey, USA) in its center for decoupling of the detection path. The mode of the detection fiber was collimated (RC04APC-P01, Thorlabs Inc.) and relayed (AC254-125-B and AC254-200-B, Thorlabs Inc.) via the rod mirror into the common Fourier plane (FP3 in Fig. 1). A 4f telescope (AC254-250-B and AC254-80-B, Thorlabs Inc.) relayed the combined illumination and detection modes to an intermediate plane between a pair of galvanometric scanners (GVS112/M, Thorlabs Inc.). A pair of achromatic doublet lenses (AC508-300-B, Thorlabs Inc.) served as an economical compound scan lens to limit the scanning-induced aberrations. An infinity-corrected tube lens (TTL200-B, Thorlabs Inc.) and a 20× plan fluorite objective lens (0.50 NA, 2.1 mm WD, N20X-PF, Nikon, Tokyo, Japan) further relayed the intermediate image plane to the object plane (OP) within the sample. Depending on the sample surface geometry, a tilted coverslip (# 1.5) was used in front of the sample to reduce specular reflection. The gap between the coverslip and the sample was filled with ultrasound gel. Typical illumination power on the sample was 7 mW.

The chromatic dispersion of the optical components in the sample arm was compensated in part by an additional 0.9 m of fiber (630HP, Thorlabs Inc., used throughout the system) in the reference arm and a pair of UV fused silica prisms (PS612, Thorlabs Inc.). Residual higher-order chromatic dispersion imbalance, induced primarily by the lithium niobate (LiNbO_3) in the EOM, was compensated numerically [35]. The reference arm power was adjusted by means of neutral density filters to reach the sensitivity plateau between receiver noise and excess noise [36].

In the detection unit, the reference light was polarized with a linear diagonal polarizer and mixed with the sample signal by a 90:10 non-polarizing beam splitter cube (BS035, Thorlabs Inc.) in favor of the sample signal. A polarizing beam splitter cube (PBS052, Thorlabs Inc.) split the combined signal into orthogonal polarization directions that were delivered via single-mode fibers to two identical spectrometers (CS800-800/300-250-OC2K-CL, Wasatch Photonics, North Carolina, USA), covering the wavelength range 650-950 nm. Of note, the polarization controller in the reference arm (PC2 in Fig. 1) was critical to match the coherence of the linear polarizations defined by polarizers P1 and P2, respectively. Whilst changing PC2 did not alter the reference power reaching the spectrometers, matching reference and sample arm polarization states optimized the fringe visibility on the spectrometer.

Two frame grabbers (Xtium-CL MX4, Teledyne Dalsa, Ontario, Canada) simultaneously acquired data from the spectrometers. Although the spectrometers support line-rates up to 250 kHz, significant excess noise of the super-continuum source imposed a modest A-line rate of 10 kHz to preserve measurement sensitivity. Synchronized frame and line trigger signals were generated together with the driving signals for the galvanometric scanners and the EOM by a control board (PC1e-6353, National Instruments, Texas, USA). A custom-written C++ application was used to control the system and display intensity tomograms of both detection channels in real-time, employing a graphics processing unit (Nvidia GeForce GTX 1080 Ti ASUS, Taipei, Taiwan) and CUDA libraries.

The typical lateral scan range for volumetric imaging was 1 mm in both the X and Y directions, defined as the fast and slow scanning lateral directions, respectively, with a range of up to 1 mm optical length, in Z, the depth coordinate. B-scans contained 3000 A-lines spaced by 0.33 μm and with alternating input polarization states, resulting in 1500 pairs of polarization-modulated A-lines. Along the Y direction, 1500 B-scans were acquired to obtain equidistant spatial intervals in the fast and slow scanning directions. Acquisition of a full volume took approximately 8 min at the available 10 kHz A-line rate.

2.2. Data processing

A standard processing chain was used to reconstruct tomograms, including fixed background removal, zeroing negative frequency content to recover the analytic signal, interpolation from pixel

to wavenumber domain, chromatic dispersion compensation, spectral reshaping and apodization, Fourier transformation to z domain, and relative sensitivity roll-off correction.

Careful relative alignment of the spectrometers' pixel to wavenumber mapping to match the spectral ranges is crucial for polarization-sensitive analysis [37]. We first calibrated the two spectrometers individually, following the method of Patarroyo *et al.* [38], which uses calibration measurements of a discrete sample reflection at varying pathlength offsets to optimize both the mapping and the dispersion imbalance. A difference in the spectral range results in diverging peak positions in the tomograms of the two spectrometers; whereas, a relative spectral offset causes a depth-dependent phase difference. Minimizing the position and phase difference between the depth-varying calibration peak signals allowed defining the pixel to wavenumber mapping of each spectrometer to ensure matching spectral ranges. The calibration data also served to characterize and compensate for relative depth-dependent signal roll-off between the two spectrometers.

Tomograms were then combined to form Jones matrix tomograms, *i.e.*, the tomograms of the two detection channels of the same A-line define a Jones vector and pairs of Jones vectors corresponding to illumination with orthogonal polarization states determine the two columns of a Jones matrix. Polarization-sensitive analysis of the Jones matrix tomograms was based on the formalism presented in our recent work [28]. It compensates for wavelength-dependent polarization distortions of the static system components and corrects for the effect of preceding tissue layers to recover the depth-resolved, *i.e.*, local, birefringence and OA orientation. In brief, recovering the intrinsic transpose symmetry of the Jones matrices served to compensate for system polarization distortions and obtain corrected Jones matrix tomograms. The amplitude of the determinant of the Jones matrix was used to define the structural image [39]. These Jones matrices encode the cumulative polarization effect of the sample, which always corresponds to the concurrent effect of a linear retarder and a linear diattenuator when using identical illumination and detection paths [28]. The linear retardation components of concurrently decomposed Jones matrices were converted to SO(3) rotation matrices and spatially averaged by a 3D Gaussian kernel with an isotropic full width at half maximum (FWHM) of 3 μm . Finally, local (*i.e.*, depth-resolved) linear SO(3) retardation matrices were recovered by recursive correction for the effect of preceding tissue layers. The amount of rotation and the angle of the rotation axis (by construction contained within the horizontal plane of the Poincaré sphere) of the local SO(3) matrix correspond to the retardation and the relative OA orientation of the local layer, respectively. The relative axis orientation between the layers is accurately recovered, but there remains an overall unknown offset in the axis orientation, which can be determined by *a priori* knowledge of the sample in many instances.

Because the effective spectral bandwidth was approximately 8 times broader than that of the conventional-resolution PS-OCT system previously used for developing the processing method [28], which resulted in a larger k -dependence of the system polarization distortions here, a few modifications of the correction method were necessary. Firstly, 29 spectral bins instead of 15 were used to estimate the correction matrices, with each bin extending over 12.5% of the full spectrum and adjacent bins overlapping with each other by 75%. Secondly, the retardation and the diattenuation vectors of the correction matrices were smoothed with a linear filter corresponding to 7% of the full spectral range, after interpolation across different spectral bins to regularize the estimation of the correction components over the full spectrum. Thirdly, to avoid a potential sign ambiguity in the Jones matrix decomposition, the linear component of the system transmission, as determined from the sample surface, was removed from the cumulative sample Jones matrices.

All processing was performed with MATLAB R2016b on a workstation PC equipped with an Intel CPU (i7-7700 @3.6GHz) and 32GB RAM. The total time to process one full volumetric dataset (500 depth pixels \times 3000 A-lines \times 1500 B-scans) was approximately 1 hour.

2.3. Sample preparation

Ocular tissues from freshly harvested adult sheep eye globes were scanned *ex vivo*. Samples were obtained through institutional tissue sharing protocols from unrelated projects that had been approved by the animal ethics committee of The University of Western Australia. Eye globes were kept in Krebs solution. When exposed to air before imaging, Krebs solution was applied to the samples to keep them hydrated. All measurements were performed within 8 hours of harvesting.

3. Results

3.1. System performance and validation

First, we set out to validate the system design and characterize its performance. The supercontinuum source, in combination with the wide-range spectrometers, offered a measured axial resolution of $1.4\ \mu\text{m}$ in air, corresponding to better than $1.0\ \mu\text{m}$ in collagen-rich samples, assuming a refractive index of $n = 1.45$ [40]. The focal properties of the decoupled illumination and detection modes are similar to our previous OCM system used for ultrahigh-resolution optical coherence elastography [31]. The annulus of the Bessel-like illumination path in the back focal plane of the sample objective lens uses an effective numerical aperture of $\text{NA}_{\text{eff}} = 0.26$; whereas, the decoupled Gaussian detection mode corresponds to $\text{NA}_{\text{eff}} = 0.14$. Combined, they offered a lateral resolution (FWHM) of $1.6\ \mu\text{m}$, extending over a $\text{DOF} \sim 70\ \mu\text{m}$, where DOF is defined as an axial OCM signal roll-off $\leq 3\ \text{dB}$. Because the detection mode rejects specular reflections of the Bessel-like illumination, system sensitivity cannot be directly measured by evaluating the signal of an attenuated reflector. Instead, system sensitivity was estimated to be $> 100\ \text{dB}$ with $7.0\ \text{mW}$ of illumination power by comparing the signal level in a scattering intralipid sample to that measured with a conventional configuration using equal Gaussian illumination and detection modes, which, in turn, allowed for traditional evaluation of system sensitivity [30].

Measuring the full Jones matrix requires combining the four tomograms obtained by the two input polarization states and the two detection channels. Ideally, the two input states would be measured in parallel, but common depth-multiplexing strategies [41,42] are challenging to implement given the limited depth-range of broadband spectrometers. Hence, we resorted to the conventional inter-A-line modulation approach. Dense lateral sampling with high spatial overlap between adjacent depth-scans of alternating input polarization states increases the fidelity of the Jones matrix measurement, but at the expense of long scanning times. To determine a suitable lateral sampling density that strikes a balance between Jones matrix fidelity and the scanning speed, we compared the degree of polarization (DOP) and the depolarization index (DI) [43] of ~ 10 times diluted coffee creamer (a lipid aqueous emulsion) imaged at different sampling densities. DOP characterizes the uniformity of the measured polarization states by analyzing spatially averaged Stokes vectors and can be computed independently from either of the two input polarization states, rendering it insensitive to the fidelity between consecutive, polarization-modulated depth-scans. Using only one of the two input states and an averaging filter with a constant spatial width resulted in a high and almost invariant $\text{DOP} > 0.9$, independent of the sampling density, as demonstrated in Fig. 2. DI, in contrast, characterizes the uniformity of the sample transmission properties by analyzing spatially averaged Mueller matrices, derived from the measured Jones matrices. Insufficient overlap between modulated depth-scans artificially limits the DI, which rises rapidly from below 0.7 to 0.85 as the sampling density increases from 400 to 3000 A-lines/mm (Fig. 2). Beyond, only a modest further increase to 0.88 was observed, suggesting 3000 A-lines/mm, or a lateral spacing of $0.33\ \mu\text{m}$ between subsequent A-lines, corresponding to $\sim 20\%$ of the measured lateral resolution, to be a reasonable sampling density.

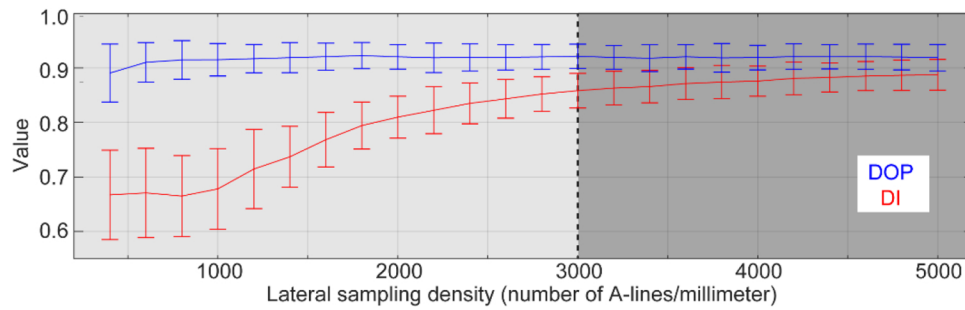


Fig. 2. Mean DOP and DI of ~10 times diluted coffee creamer with respect to the lateral A-line sampling density. DOP, degree of polarization; DI, depolarization index. The error bars represent standard deviation. The change in shading highlights the chosen value of sampling density for imaging.

To validate birefringence imaging with the high-resolution, focus-extended PS-OCM system, we measured a polylactic acid (PLA) birefringence phantom that we also imaged with our lower-resolution PS-OCT system operating at 1310 nm central wavelength [28,44]. The local retardation measured in matching areas ($300\ \mu\text{m} \times 150\ \mu\text{m}$, XZ) was in the interquartile range of $0.60 - 1.30\ \text{deg}/\mu\text{m}$ and $0.35 - 0.75\ \text{deg}/\mu\text{m}$, using the PS-OCM and PS-OCT system, respectively. Computing absolute birefringence to account for the different central wavelengths resulted in excellent agreement between the two systems: birefringence in the range $0.65 \times 10^{-3} - 1.41 \times 10^{-3}$ and $0.64 \times 10^{-3} - 1.36 \times 10^{-3}$, respectively. The same phantom was also measured at different OA orientation angles, and the calculated mean relative local OA orientation was in close agreement with the set angle ($R^2 = 0.98$).

3.2. Corneal-scleral limbus of sheep eye

The high resolution of OCM and also of full-field OCT has previously been used to assess the micromorphology of the cornea [17,20]. In line with these previous reports, structural images of the corneal-scleral limbus of a sheep eye measured *ex vivo* revealed rich morphological features. A representative cross-section acquired along the fast scanning direction (XZ) is displayed in Fig. 3(a), transitioning from the sclera (left) to the cornea (right). Stronger scattering differentiates the stroma from the epithelium. The distinct layer covering the sclera is likely Tenon's capsule, overlying the periscleral lymph space with several vessels clearly visible. The stroma appears as a homogeneously scattering body, interspersed only by stromal striae that present as vertically oriented shadow-like structures [45]; three representative examples are marked by the red asterisks in Fig. 3(a). Whilst high for OCT imaging, the achieved spatial resolution is insufficient to reveal any detail on the internal organization of the stroma. The lamellar architecture of the stroma, consisting of sheets or strips of aligned collagen fibrils that have distinct, seemingly random orientations parallel to the corneal surface, has been well established using microscopy techniques, including PLM and SHG microscopy [46], but remains inaccessible to OCT and OCM.

Figure 3(b) displays the local OA map corresponding to the same cross-section using a 2D color map, encoding the local OA orientation in color and the local retardation, after a further spatial filtering with a kernel of approximately twice the size of the speckle, in brightness. The OA map reveals thin, clearly defined, at times wavy, layers of distinct OA orientation that are entirely indistinguishable in the structural intensity image. The local OA indicates the angular direction of linear polarization, within the plane orthogonal to the interrogating beam, that experiences the fastest propagation. In the case of fibrillar collagen, this corresponds to the

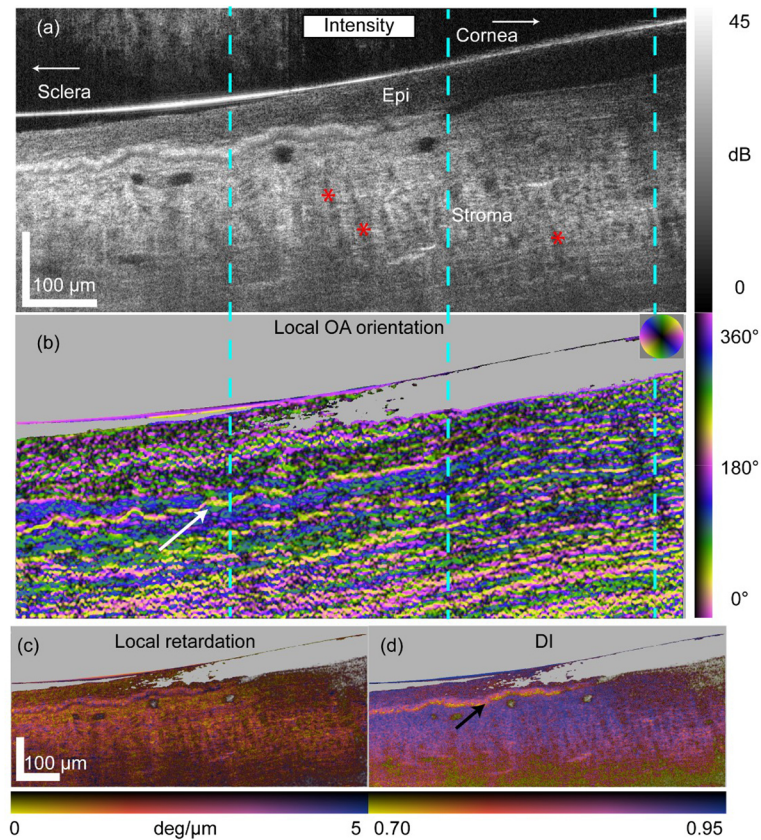


Fig. 3. A representative cross-sectional view (in the fast scanning direction, XZ) of the intensity (a), local OA orientation (b), local retardation (c), and DI (d), of the corneal-sclera limbus region of an adult sheep eye globe (Sample #1), imaged *ex vivo*. Epi, epithelium; OA, optic axis; DI, depolarization index. The local OA orientation image is color coded and overlaid with the local retardation as brightness, as indicated by the color bar and wheel in panel (b). The red asterisks in (a) indicate three representative stromal striae. The dashed cyan lines in (a) and (b) correspond to the cross-sections in the slow scanning direction (YZ), shown in Fig. 4. The white arrow in (b) and the white arrow in Fig. 4(a) highlight the same OA layer in orthogonal cross-sections. The black arrow in (d) indicates a high depolarizing layer, presumed to be Tenon's capsule. A fly-through video of the volumetric data (1.0 mm \times 1.0 mm \times 0.45 mm, XYZ) is available as [Visualization 1](#). Scale bars: 100 μ m.

direction orthogonal to the fiber orientation and suggests that consecutive layers have very distinct fiber orientation, as expected from the individual lamellae. Because of the unknown overall offset, it is possible, however, to treat the OA orientation as the fiber orientation. On the left-hand side of the image in the sclera, layer thickness is heterogeneous, with some very thin layers sandwiched between thicker layers. In the cornea on the right-hand side, the layers appear uniformly thin. Interestingly, the striae, while clearly visible in the scattering signal, have little impact on the OA signal and are invisible in the OA maps. Reconstructing the local OA corrects for the cumulative polarization rotating effect of preceding layers, but there remains an overall unknown orientation offset, leaving the absolute 0° direction undefined. Also, depth-correction is only possible with sufficient signal and areas with low SNR (< 7 dB in the stroma and < 15 dB in the epithelium) are, thus, grayed out. Furthermore, the OA is only meaningful in areas with sufficient local

retardation. Indeed, where not masked, the OA orientation in the epithelium and other tissue ahead of the stroma appears random, with two dominating apparent OA orientations encoded in green and purple, respectively, but without defining layers of continuous OA orientation. A fly-through video of the micro-morphology and the local OA orientation of the entire volume ($1 \text{ mm} \times 1 \text{ mm} \times 0.45 \text{ mm}$, XYZ) is available as [Visualization 1](#).

Figure 3(c) shows the local retardation, overlaid with the intensity image as brightness. Whilst the range of local retardation values is high for biological samples, the local retardation image exhibits only poor contrast and does not reveal any clear features. Figure 3(d) displays the DI, in a similar overlay with the intensity image. As well as an obvious noise-induced depolarization noticeable at deeper sample locations, Tenon's capsule induces pronounced depolarization, indicated by the black arrow in (d).

To further illustrate the change in thickness of the observed layers between the sclera and the cornea, Fig. 4 presents cross-sectional views of the same volumetric data along the slow scanning direction (YZ), taken at the positions of the dashed cyan lines in Figs. 3(a) and (b), respectively. A fly-through video of the volumetric data ($1 \text{ mm} \times 1 \text{ mm} \times 0.45 \text{ mm}$, XYZ) in this orientation is available as [Visualization 2](#), highlighting the smooth transition in layer thickness from the sclera to the cornea. Leveraging the distinct advantage of volumetric imaging over histology, we point out one interesting fiber bundle, i.e., the yellow layer marked by the white arrow in Fig. 3(b) and Fig. 4(a). It extends over almost $500 \mu\text{m}$ of the trans-ocular cross-section in Fig. 3(b) but has a shorter width of approximately $200 \mu\text{m}$ in Fig. 4(a), suggesting a radial orientation of this particular strip. From this observation, it can be inferred that the yellow color in the local OA orientation points to the center of the cornea; whereas, the blue color is orthogonal, i.e., in the azimuthal direction.

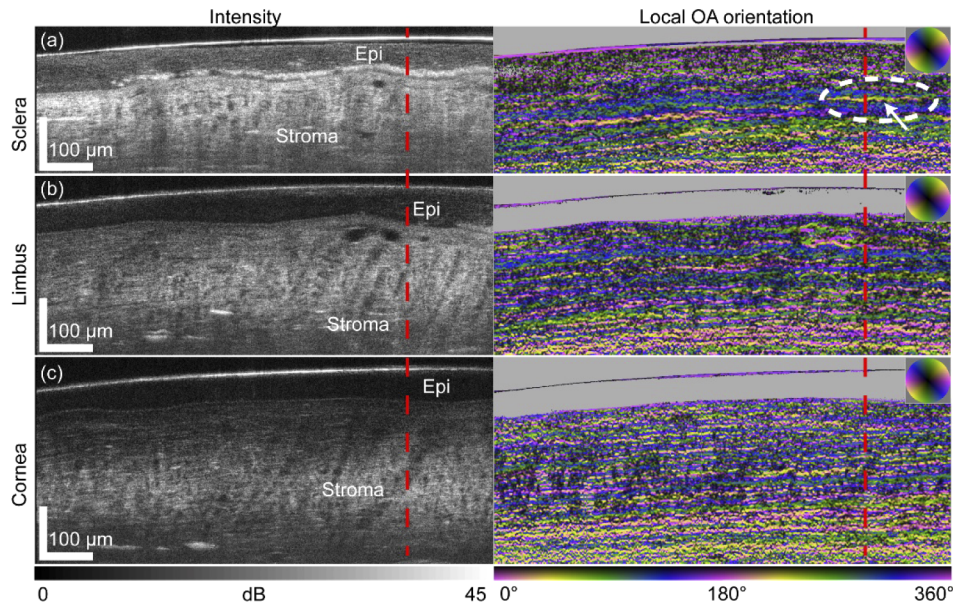


Fig. 4. Three representative cross-sectional views (in the slow scanning direction, YZ) of the intensity (left column) and local OA orientation (right column) of Sample #1. (a-c) are from the sclera, limbus and cornea, respectively, corresponding to the dashed cyan lines in Figs. 3(a) and (b), from left to right. The dashed red lines correspond to the cross-section in Fig. 3. The white arrow and dashed ellipse in (a) and the white arrow in Fig. 3(b) highlight the same OA layer in orthogonal cross-sections. Epi, epithelium. A fly-through video of the volumetric data ($1 \text{ mm} \times 1 \text{ mm} \times 0.45 \text{ mm}$, XYZ) is available as [Visualization 2](#). Scale bars: $100 \mu\text{m}$.

A representative cross-sectional view of the intensity and the local OA orientation of the limbus region imaged in a second sample is presented in Fig. 5. In this sample, the individual layers in the stroma form more complex networks than observed in the first sample, suggesting possible fusing and branching [1]. Again, nothing in the structural images discloses this intricate internal organization that is only revealed by the local OA image, and best appreciated in the fly-through video of the volumetric data (1 mm × 0.5 mm × 0.54 mm, XYZ), available as [Visualization 3](#).

Overall, conventional backscatter tomograms and local retardation images (not shown) of the stromal tissue in the limbus region of sheep eyes provide valuable image contrast but do not reveal the detailed tissue organization related to the directional arrangement of fibrillar tissue components. In comparison, the local OA orientation maps exhibit striking contrast and reveal individual layers with distinct orientation, consistent with the known lamellar architecture of the cornea and sclera.

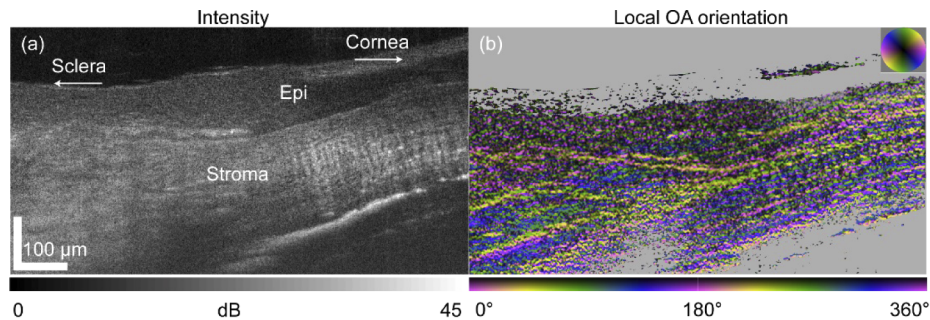


Fig. 5. A representative B-scan view of the intensity (a) and the local OA orientation (b) of the limbus region of an adult sheep eye globe (Sample #2), imaged *ex vivo*. Epi, epithelium. A fly-through video of the volumetric data (1 mm × 0.5 mm × 0.54 mm, XYZ) is available as [Visualization 3](#). Scale bars: 100 μm.

3.3. Anterior stroma of sheep cornea

Whereas the limbus serves well to demonstrate the OA contrast available with focus-extended PS-OCM, more emphasis is generally placed on the collagen structure in the center of the cornea, where abnormalities carry direct implications for visual acuity. Hence, we imaged the central region of the anterior stroma of the cornea in a fresh and intact adult sheep eye globe *ex vivo*. The focus of the imaging beam was placed slightly inside the anterior stroma. Two representative cross-sectional views of the intensity and the local OA, in the fast scanning (XZ) and slow scanning (YZ) directions, are presented in Figs. 6(a) and (b), respectively. The backscatter signal in this central part of the cornea appears even more homogeneous than in the limbus region. The local OA images, in comparison, reveal rich contrast with alternating distinctly oriented layers. In the superficial region, layers are more loosely arranged and not strictly parallel to the corneal surface. Starting from the middle of the imaged depth in the stroma, the sheets form more parallel and continuous lamellae. This observation is in line with investigations using SHG microscopy [47]. A fly-through video of the volumetric data (0.8 mm × 0.8 mm × 0.26 mm, XYZ) is available as [Visualization 4](#).

3.4. Posterior stroma of sheep cornea

Lastly, we dissected the entire cornea of a fresh adult sheep eye globe and imaged the posterior stroma from the inside out, by directly attaching the inner side of the cornea, *i.e.*, the endothelium, to a microscope coverslip, with the help of ultrasound gel. The dissected cornea is pliable and

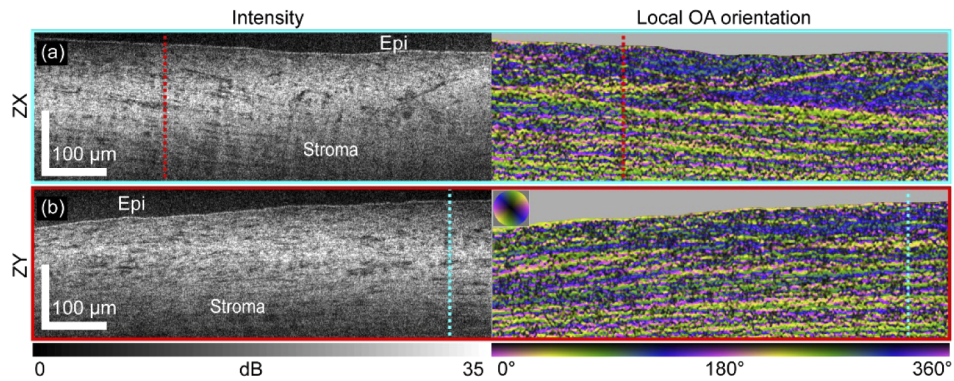


Fig. 6. Cross-sectional views of intensity (left column) and local OA orientation (right column) of the anterior stroma of the cornea of an *ex-vivo* adult sheep eye globe, in the fast (XZ) (a) and slow (YZ) (b) scanning directions, respectively. (a) corresponds to the cyan dashed lines in (b), and (b) corresponds to the red dashed lines in (a). Epi, epithelium. A fly-through video of the volumetric data ($0.8 \text{ mm} \times 0.8 \text{ mm} \times 0.26 \text{ mm}$, XYZ) in the fast scanning direction (XZ) is available as [Visualization 4](#). Scale bars: $100 \mu\text{m}$.

although it was not flattened, the geometry of the sample seen here in OCM may not represent its original shape.

A cross-sectional view of the intensity and the local OA is presented in Fig. 7. The hyperscattering horizontal structures correspond to keratocytes that mostly lie in between lamellae [48,49] and hence provide an indication of lamellar borders, but generally the axial resolution remains insufficient to distinguish individual lamellae based on scattering contrast,

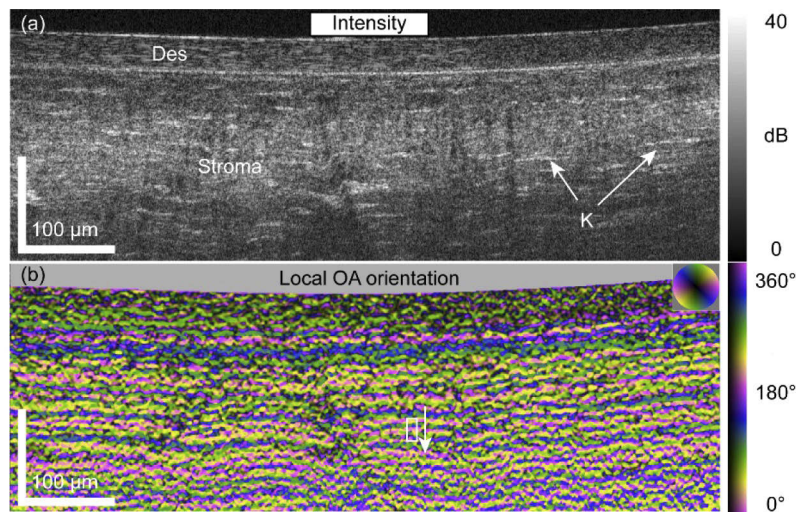


Fig. 7. A representative cross-sectional view (in the fast scanning direction, XZ) of the intensity (a) and local OA orientation (b) of the posterior stroma of the dissected cornea from a sheep eye globe, imaged at approximately the central region, from inside out *ex vivo*. Des, Descemet's membrane; K, keratocytes. Two representative keratocytes are indicated by white arrows in (a). The lamellae corresponding to the central A-line in the white box in (b) were analyzed and plotted in Fig. 8. A fly-through video of the volumetric data ($0.8 \text{ mm} \times 0.8 \text{ mm} \times 0.29 \text{ mm}$, XYZ) is available as [Visualization 5](#).

unlike the OA orientation, which reveals tightly stacked, parallel layers, suggestive of lamellae. The thick Descemet's membrane seen here is consistent with the histology of sheep eyes [50,51]. A fly-through video of the volumetric data ($0.8 \text{ mm} \times 0.8 \text{ mm} \times 0.29 \text{ mm}$, XYZ) is available as [Visualization 5](#), which suggests that although the lamellae form small domains and, therefore, appear wavy, they are continuous, even across striae.

Figure 8 presents a detailed analysis of the thickness and relative orientation of a depth-scan across five representative consecutive lamellae, indicated by the white box in Fig. 7(b). Each pixel in depth is $1.0 \text{ }\mu\text{m}$ in optical pathlength and $\sim 0.7 \text{ }\mu\text{m}$ in physical length. Due to the averaging effect of both the physical measurement and the processing, the local retardation is lowest at the interface between adjacent lamellae and coincides with a change in the local OA orientation, as clearly evident in Fig. 8(a). Using polar coordinates to visualize both the retardation and the orientation of the local OA further clarifies the OA evolution across individual lamellae. On average, each lamella measures 7 pixels in depth, which corresponds to a physical thickness of $\sim 4.9 \text{ }\mu\text{m}$. The orientation between adjacent lamellae changes by $\sim 80^\circ$, except for a smaller change of only $\sim 60^\circ$ between the 3rd and the 4th layer. We conclude that adjacent lamellae have random orientation relative to each other, in agreement with observations using SHG microscopy [11,52].

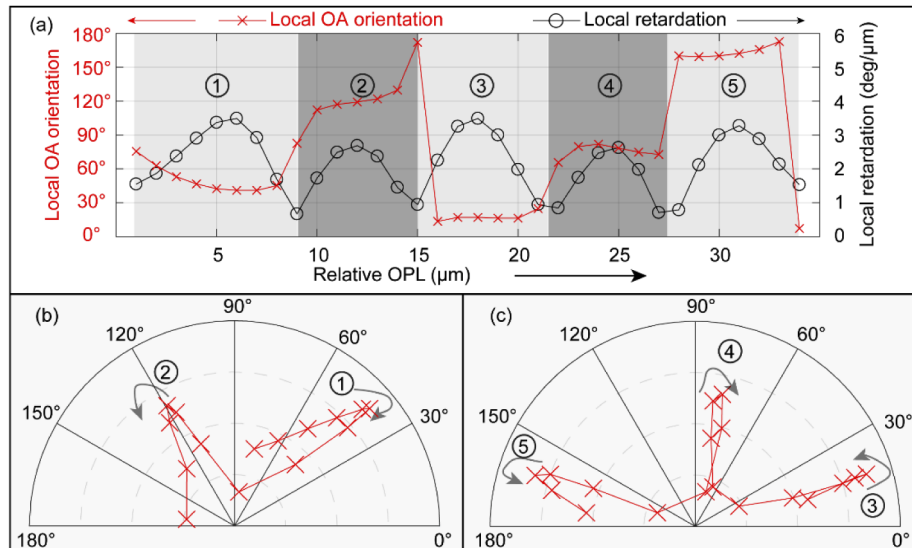


Fig. 8. A quantitative analysis of local OA orientation and local retardation in five representative lamellae in the posterior stroma. (a) Plot of the local OA orientation and the local retardation in a short segment of a representative A-line, located in the center of the white box in Fig. 7(b). Five lamellae are distinguished in this range. OPL, optical path length. (b),(c) Plots of the vectorized local OA orientation and local retardation of the five lamellae in polar coordinates, where the local OA orientation and local retardation are represented as the angle and the length of the vectors, respectively. In (b) and (c), the radius of the semicircles represents $4.0 \text{ deg}/\mu\text{m}$ of local retardation.

4. Discussion

This study demonstrates the striking contrast of local OA imaging when combined with the improved spatial resolution of OCM. Depending on the specific tissue morphology, scattering contrast may be sufficient to reveal relevant details at high spatial resolution, as in the coronary arteries [53] or for imaging of Alzheimer's plaques [54]. In the cornea, OCM resolves fine details

including nerves, keratocytes, and stromal striae, but detecting the orientation of collagen fibers and inspecting their microscopic arrangement remains difficult simply based on spatially resolved measurements of the amplitude of backscattered light. However, the orientation of collagen fibers induces minute polarization-dependent phase differences in the backscattered light, which we utilize to reconstruct the local OA orientation from polarization-sensitive measurements. As evidenced with focus-extended PS-OCM images of the limbus and cornea, local OA images offer an impressive contrast between adjacent tissue layers that only differ in their orientation and are indistinguishable in structural tomograms. Similarly, the scalar amount of local retardation proved difficult to interpret, likely because the layers feature comparable local retardation and only contrast in their OA orientation. Previous measurements of human sclera with lower resolution in the $1.3\text{ }\mu\text{m}$ wavelength region have resulted in much lower local retardation values ($<1\text{ deg}/\mu\text{m}$) [55], even when considering the difference in wavelength. Our higher retardation values ($\sim 3\text{ deg}/\mu\text{m}$) are likely the result of the improved spatial resolution, which reduces the extent of averaging across several differently oriented collagen fibers.

To the best of our knowledge, this work is the first demonstration of high-resolution local OA imaging. Previous efforts combining PS-OCT with the high resolution of OCM used cumulative OA imaging of brain tissue [56,57]. The correction for system polarization distortions and the reconstruction of the local instead of the cumulative OA orientation employed in the current work were critical to obtain the presented results. The polarization states across the wide wavelength range required to achieve high axial resolution are bound to experience spectrally dependent variations upon propagation through the system components, leading to artifacts in the reconstructed OA and birefringence maps.

Indeed, in conventional retinal PS-OCT, the transmission through the cornea only imparts a modest polarization change on the imaging beam that can be compensated [58]. Direct investigation of the cumulative retardation and OA of the cornea exhibits characteristic patterns exceeding a quarter-wave of retardation and has been shown to differ in keratoconus patients [59]. The extent to which the angle of incidence on the corneal surface impacts the observed retardation effects remains a topic of investigation [60]. On the macroscopic scale, the cumulative retardation across the full thickness of the cornea, consisting of a stack of thin lamellae with random orientations, can be expected to be modest. Although each lamella exhibits moderate birefringence, an adjacent lamella with an OA oriented at 90° entirely compensates the retardation across the pair of lamellae. The more random angular orientation reported from mammalian corneas [52] still results, overall, in the absence of any pronounced retardation. However, inspecting the corneal polarization properties with the improved spatial resolution of our focus-extended PS-OCM displays a dramatically different picture. The observed OA patterns of distinctly oriented layers closely match the expected organization of stromal tissue into tightly stacked lamellae. The estimated layer thickness of $\sim 4.9\text{ }\mu\text{m}$ is consistent with reports of transmission electron microscopy of adult sheep cornea [51], although literature values for lamellar thickness in human cornea are smaller [61]. Currently, our results lack comparison with histopathology confirming a direct association of the observed OA layers with individual lamellae. Future studies are needed to examine if the resolution of focus-extended PS-OCM is sufficient to resolve lamellae in human cornea.

A further limitation of our work is the investigation of excised eye globes *ex vivo*. Previous studies of PS-OCT in the cornea suggested specific depolarization signatures only arise *in vivo* [60]. It remains an open question if and how this would impact local OA imaging. There is no fundamental barrier to performing focus-extended PS-OCM *in vivo*. In this initial investigation of combining local OA imaging with OCM, the high relative intensity noise of the available supercontinuum source limited the acquisition speed. Newer sources with higher pump repetition rates have been shown to allow OCT operation with a 70 kHz A-line rate in the shot-noise limit [62]. Depth-encoding the two input polarization states instead of sequential modulation would

relieve the tight spatial sampling constraint and enable faster and more flexible scanning. The implemented focus scheme already ensures that a tight lateral resolution can be maintained over an extended axial range and avoids the multiple acquisitions with varied axial focus positions of conventional OCM [63,64]. Although the nominal DOF, defined as the FWHM of the product of the intensity profiles of the illuminating Bessel beam and the detecting Gaussian beam, is only approximately 70 μm , the practical imaging range providing meaningful intensity images and OA orientation maps extends well beyond 300 μm . The long tail of the Bessel-like illumination results in a slow decay of the illumination power behind the focus position, maintaining an appreciable signal beyond the nominal DOF. In the intensity images, the logarithmic display helps to produce an appreciable gray-level at these depth positions. The OA maps depend primarily on the SNR, and hence benefit from the same extended range. Combination with numerical refocusing may enable imaging through the entire cornea, since it would potentially enable one to correct for aberrations that limit the imaging depth in tissue achievable at high resolution [65].

There remains room for improving the local OA reconstruction method. Currently, the compensation for the preceding tissue layers occurs recursively, starting from the sample surface. When focusing deeper inside a sample, the surface signal may have limited SNR and only provide a poor starting point for this correction. In these situations, we started from a higher SNR area within the sample but lost the surface reference that would be needed when attempting to convert the relative to absolute OA orientations. Also, the processing assumes that polarization-dependent scattering amplitude, *i.e.*, diattenuation, is negligible and casts the measurements into the SO(3) formalism. Whilst static system diattenuation is corrected by our processing before conversion to the SO(3) formalism, we found that its presence makes the noise polarization-dependent, and causes preferential OA directions in noise-dominated regions with low birefringence. This explains the observed OA pattern in the epithelium and the Descemet's membrane, which are both cellular and not fibrillar structures. A more rigorous strategy to treat system diattenuation and consider sample diattenuation and depolarization effects may achieve improved results and reveal additional sample features.

We highlighted the remarkable opportunities for high-resolution OA imaging by inspecting structures in the anterior eye. Such imaging could be of particular interest for the study and diagnosis of keratoconus, which involves alterations in the collagen lamellae and fibrils [66,67], leading to a loss of the normal interwoven structure of the lamellae [68,69]. Whereas current diagnostic strategies, including Brillouin microscopy [14], probe the biomechanical properties of the thinning cornea, OA imaging may offer direct insight into the altered collagen morphology. Besides the anterior eye, there are numerous tissues with similarly intricate fibrillar architectures. Further progress in local OA imaging, in combination with the high spatial resolution of OCM, may enable the investigation of the skin, nerves, vessel walls, or cartilage *in vivo* on the microscopic scale, which remains difficult to date.

5. Conclusions

Vectorial birefringence enables detailed study of the organization of intact fibrillar tissues, probing tissue organization on length scales beyond the imaging resolution. Our results demonstrate that the improved spatial resolution of focus-extended PS-OCM is critical to avoid averaging of the birefringence features and to resolve relevant morphological features. Whereas tomograms of the backscatter-intensity and the scalar amount of local birefringence fail to reliably differentiate individual lamellar layers in sheep cornea, the local OA orientation reveals distinct layers with striking contrast, suggesting that the vectorial property of birefringence is more resilient to the detrimental averaging effects of limited spatial resolution. The same contrast enhancement may enable human *in vivo* imaging, with suitable improvements in the imaging speed, for investigation of the cornea or other organs accessible to OCM imaging.

Funding

Australian Research Council (DP160104969); National Institutes of Health (P41EB-015903, R03EB-024803); Western Australian Department of Health Merit Award and the Medical and Health Research Infrastructure Fund.

Acknowledgements

The authors acknowledge Dr. Andrea Curatolo, Dr. Danuta Sampson, Prof. Dao-Yi Yu, Dr. Peijun Gong, Dr. Nishant Mohan, Prof. Chulmin Joo and Dr. Boy Braaf for fruitful discussions. Q. Li acknowledges the financial support of the Australian Government International Research Training Program (RTP) Fee Offset Scholarships.

Disclosures

The authors declare that there are no conflicts of interest related to this article.

References

1. K. M. Meek and C. Knupp, "Corneal structure and transparency," *Prog. Retinal Eye Res.* **49**, 1–16 (2015).
2. S. Yamamoto, H. Hashizume, J. Hitomi, M. Shigeno, S. Sawaguchi, H. Abe, and T. Ushiki, "The subfibrillar arrangement of corneal and scleral collagen fibrils as revealed by scanning electron and atomic force microscopy," *Arch. Histol. Cytol.* **63**(2), 127–135 (2000).
3. W. Radner, M. Zehetmayer, R. Aufreiter, and R. Mallinger, "Interlacing and cross-angle distribution of collagen lamellae in the human cornea," *Cornea* **17**(5), 537–543 (1998).
4. K. M. Meek and C. Boote, "The use of X-ray scattering techniques to quantify the orientation and distribution of collagen in the corneal stroma," *Prog. Retinal Eye Res.* **28**(5), 369–392 (2009).
5. K. M. Meek and A. J. Quantock, "The use of X-ray scattering techniques to determine corneal ultrastructure," *Prog. Retinal Eye Res.* **20**(1), 95–137 (2001).
6. N.-J. Jan, J. L. Grimm, H. Tran, K. L. Lathrop, G. Wollstein, R. A. Bilonick, H. Ishikawa, L. Kagemann, J. S. Schuman, and I. A. Sigal, "Polarization microscopy for characterizing fiber orientation of ocular tissues," *Biomed. Opt. Express* **6**(12), 4705–4718 (2015).
7. N.-J. Jan, B. L. Brazile, D. Hu, G. Grube, J. Wallace, A. Gogola, and I. A. Sigal, "Crimp around the globe; patterns of collagen crimp across the corneoscleral shell," *Exp. Eye Res.* **172**, 159–170 (2018).
8. B. Yang, N.-J. Jan, B. Brazile, A. Voorhees, K. L. Lathrop, and I. A. Sigal, "Polarized light microscopy for 3-dimensional mapping of collagen fiber architecture in ocular tissues," *J. Biophotonics* **11**, e201700356 (2018).
9. Y. Mega, M. Robitaille, R. Zareian, J. McLean, J. Ruberti, and C. DiMarzio, "Quantification of lamellar orientation in corneal collagen using second harmonic generation images," *Opt. Lett.* **37**(16), 3312–3314 (2012).
10. S.-W. Teng, H.-Y. Tan, J.-L. Peng, H.-H. Lin, K. H. Kim, W. Lo, Y. Sun, W.-C. Lin, S.-J. Lin, S.-H. Jee, P. T. C. So, and C.-Y. Dong, "Multiphoton autofluorescence and second-harmonic generation imaging of the *ex vivo* porcine eye," *Invest. Ophthalmol. Visual Sci.* **47**(3), 1216–1224 (2006).
11. G. Latour, I. Gusachenko, L. Kowalczyk, I. Lamarre, and M.-C. Schanne-Klein, "In vivo structural imaging of the cornea by polarization-resolved second harmonic microscopy," *Biomed. Opt. Express* **3**(1), 1–15 (2012).
12. G. Scarcelli and S. H. Yun, "In vivo Brillouin optical microscopy of the human eye," *Opt. Express* **20**(8), 9197–9202 (2012).
13. G. Scarcelli and S. H. Yun, "Confocal Brillouin microscopy for three-dimensional mechanical imaging," *Nat. Photonics* **2**(1), 39–43 (2008).
14. T. G. Seiler, P. Shao, A. Eltony, T. Seiler, and S.-H. Yun, "Brillouin spectroscopy of normal and keratoconus corneas," *Am. J. Ophthalmol.* **202**, 118–125 (2019).
15. M. Ang, M. Baskaran, R. M. Werkmeister, J. Chua, D. Schmidl, V. Aranha dos Santos, G. Garhöfer, J. S. Mehta, and L. Schmetterer, "Anterior segment optical coherence tomography," *Prog. Retinal Eye Res.* **66**, 132–156 (2018).
16. J. L. B. Ramos, Y. Li, and D. Huang, "Clinical and research applications of anterior segment optical coherence tomography – a review," *Clin. Experiment. Ophthalmol.* **37**(1), 81–89 (2009).
17. R. M. Werkmeister, S. Sapeta, D. Schmidl, G. Garhöfer, G. Schmidinger, V. Aranha dos Santos, G. C. Aschinger, I. Baumgartner, N. Pircher, F. Schwarzgans, A. Pantalon, H. Dua, and L. Schmetterer, "Ultrahigh-resolution OCT imaging of the human cornea," *Biomed. Opt. Express* **8**(2), 1221–1239 (2017).
18. K. Bizheva, B. Tan, B. MacLellan, O. Kralj, M. Hajialamdari, D. Hileeto, and L. Sorbara, "Sub-micrometer axial resolution OCT for *in-vivo* imaging of the cellular structure of healthy and keratoconic human corneas," *Biomed. Opt. Express* **8**(2), 800–812 (2017).
19. B. Tan, Z. Hosseinaee, L. Han, O. Kralj, L. Sorbara, and K. Bizheva, "250 kHz, 1.5 μ m resolution SD-OCT for *in-vivo* cellular imaging of the human cornea," *Biomed. Opt. Express* **9**(12), 6569–6583 (2018).

20. V. Mazlin, P. Xiao, E. Dalimier, K. Grieve, K. Irsch, J.-A. Sahel, M. Fink, and A. C. Boccara, "In vivo high resolution human corneal imaging using full-field optical coherence tomography," *Biomed. Opt. Express* **9**(2), 557–568 (2018).
21. R. Oldenbourg, "A new view on polarization microscopy," *Nature* **381**(6585), 811–812 (1996).
22. R. A. Carlton, "Polarized Light Microscopy," in *Pharmaceutical Microscopy*, R. A. Carlton, ed. (Springer New York, New York, NY, 2011), pp. 7–64.
23. J. F. de Boer, C. K. Hitzenberger, and Y. Yasuno, "Polarization sensitive optical coherence tomography - a review [Invited]," *Biomed. Opt. Express* **8**(3), 1838–1873 (2017).
24. B. Baumann, "Polarization sensitive optical coherence tomography: A review of technology and applications," *Appl. Sci.* **7**(5), 474 (2017).
25. C. Fan and G. Yao, "Mapping local optical axis in birefringent samples using polarization-sensitive optical coherence tomography," *J. Biomed. Opt.* **17**(11), 110501 (2012).
26. C. Fan and G. Yao, "Imaging myocardial fiber orientation using polarization sensitive optical coherence tomography," *Biomed. Opt. Express* **4**(3), 460–465 (2013).
27. M. Villiger, B. Braaf, N. Lippok, K. Otsuka, S. K. Nadkarni, and B. E. Bouma, "Optic axis mapping with catheter-based polarization-sensitive optical coherence tomography," *Optica* **5**(10), 1329–1337 (2018).
28. Q. Li, K. Karnowski, P. B. Noble, A. Cairncross, A. James, M. Villiger, and D. D. Sampson, "Robust reconstruction of local optic axis orientation with fiber-based polarization-sensitive optical coherence tomography," *Biomed. Opt. Express* **9**(11), 5437–5455 (2018).
29. R. A. Leitgeb, M. Villiger, A. H. Bachmann, L. Steinmann, and T. Lasser, "Extended focus depth for Fourier domain optical coherence microscopy," *Opt. Lett.* **31**(16), 2450–2452 (2006).
30. M. Villiger, C. Pache, and T. Lasser, "Dark-field optical coherence microscopy," *Opt. Lett.* **35**(20), 3489–3491 (2010).
31. A. Curatolo, M. Villiger, D. Lorenser, P. Wijesinghe, A. Fritz, B. F. Kennedy, and D. D. Sampson, "Ultrahigh-resolution optical coherence elastography," *Opt. Lett.* **41**(1), 21–24 (2016).
32. C. E. Saxer, J. F. de Boer, B. H. Park, Y. Zhao, Z. Chen, and J. S. Nelson, "High-speed fiber-based polarization-sensitive optical coherence tomography of *in vivo* human skin," *Opt. Lett.* **25**(18), 1355–1357 (2000).
33. B. H. Park, M. C. Pierce, B. Cense, and J. F. de Boer, "Real-time multi-functional optical coherence tomography," *Opt. Express* **11**(7), 782–793 (2003).
34. D. Lorenser, C. Christian Singe, A. Curatolo, and D. D. Sampson, "Energy-efficient low-Fresnel-number Bessel beams and their application in optical coherence tomography," *Opt. Lett.* **39**(3), 548–551 (2014).
35. M. Wojtkowski, V. J. Srinivasan, T. H. Ko, J. G. Fujimoto, A. Kowalczyk, and J. S. Duker, "Ultrahigh-resolution, high-speed, Fourier domain optical coherence tomography and methods for dispersion compensation," *Opt. Express* **12**(11), 2404–2422 (2004).
36. J. F. de Boer, R. Leitgeb, and M. Wojtkowski, "Twenty-five years of optical coherence tomography: the paradigm shift in sensitivity and speed provided by Fourier domain OCT [Invited]," *Biomed. Opt. Express* **8**(7), 3248–3280 (2017).
37. M. Mujat, B. H. Park, B. Cense, T. C. Chen, and J. F. de Boer, "Autocalibration of spectral-domain optical coherence tomography spectrometers for *in vivo* quantitative retinal nerve fiber layer birefringence determination," *J. Biomed. Opt.* **12**(4), 041205 (2007).
38. N. Uribe-Patarroyo, S. H. Kassani, M. Villiger, and B. E. Bouma, "Robust wavenumber and dispersion calibration for Fourier-domain optical coherence tomography," *Opt. Express* **26**(7), 9081–9094 (2018).
39. J. Li and J. F. de Boer, "Coherent signal composition and global phase determination in signal multiplexed polarization sensitive optical coherence tomography," *Opt. Express* **22**(18), 21382–21392 (2014).
40. A. N. Bashkatov, E. A. Genina, V. I. Kochubey, and V. V. Tuchin, "Estimation of wavelength dependence of refractive index of collagen fibers of scleral tissue," *Proc. SPIE* **4162**, 265–268 (2000).
41. B. Baumann, W. Choi, B. Potsaid, D. Huang, J. S. Duker, and J. G. Fujimoto, "Swept source / Fourier domain polarization sensitive optical coherence tomography with a passive polarization delay unit," *Opt. Express* **20**(9), 10229–10241 (2012).
42. Y. Lim, Y.-J. Hong, L. Duan, M. Yamanari, and Y. Yasuno, "Passive component based multifunctional Jones matrix swept source optical coherence tomography for Doppler and polarization imaging," *Opt. Lett.* **37**(11), 1958–1960 (2012).
43. N. Lippok, M. Villiger, and B. E. Bouma, "Degree of polarization (uniformity) and depolarization index: unambiguous depolarization contrast for optical coherence tomography," *Opt. Lett.* **40**(17), 3954–3957 (2015).
44. J. Walther, Q. Li, M. Villiger, C. S. Farah, E. Koch, K. Karnowski, and D. D. Sampson, "Depth-resolved birefringence imaging of collagen fiber organization in the human oral mucosa *in vivo*," *Biomed. Opt. Express* **10**(4), 1942–1956 (2019).
45. K. Grieve, D. Ghoubay, C. Georgeon, G. Latour, A. Nahas, K. Plamann, C. Crotti, R. Bocheux, M. Borderie, T.-M. Nguyen, F. Andreiulo, M.-C. Schanne-Klein, and V. Borderie, "Stromal striae: a new insight into corneal physiology and mechanics," *Sci. Rep.* **7**(1), 13584 (2017).
46. M. Winkler, D. Chai, S. Krilling, C. J. Nien, D. J. Brown, B. Jester, T. Juhasz, and J. V. Jester, "Nonlinear optical macroscopic assessment of 3-D corneal collagen organization and axial biomechanics," *Invest. Ophthalmol. Visual Sci.* **52**(12), 8818–8827 (2011).
47. N. Morishige, Y. Takagi, T. Chikama, A. Takahara, and T. Nishida, "Three-dimensional analysis of collagen lamellae in the anterior stroma of the human cornea visualized by second harmonic generation imaging microscopy," *Invest. Ophthalmol. Visual Sci.* **52**(2), 911–915 (2011).

48. J. A. West-Mays and D. J. Dwivedi, "The keratocyte: Corneal stromal cell with variable repair phenotypes," *Int. J. Biochem. Cell Biol.* **38**(10), 1625–1631 (2006).
49. G. H.-F. Yam, G. P. Williams, M. Setiawan, N. Z. B. M. Yusoff, X.-w. Lee, H. M. Htoon, L. Zhou, M. Fuest, and J. S. Mehta, "Nerve regeneration by human corneal stromal keratocytes and stromal fibroblasts," *Sci. Rep.* **7**(1), 45396 (2017).
50. C. A. Greene, S. L. Misra, H. Lee, J. McKelvie, K. Kapadia, R. McFarlane, C. N. J. McGhee, C. R. Green, and T. Sherwin, "The sheep cornea: structural and clinical characteristics," *Curr. Eye Res.* **43**(12), 1432–1438 (2018).
51. T. A. Cafaro, M. F. Suarez, C. Maldonado, J. O. Croxatto, C. Insfrán, J. A. Urrets-Zavalía, and H. M. Serra, "On the cornea of healthy merino sheep: a detailed *ex vivo* confocal, histological and ultrastructural study," *Anat. Histol. Embryol.* **44**(4), 247–254 (2015).
52. M. Winkler, G. Shoa, S. T. Tran, Y. Xie, S. Thomasy, V. K. Raghunathan, C. Murphy, D. J. Brown, and J. V. Jester, "A comparative study of vertebrate corneal structure: The evolution of a refractive lensvertebrate corneal structure," *Invest. Ophthalmol. Visual Sci.* **56**(4), 2764–2772 (2015).
53. L. Liu, J. A. Gardecki, S. K. Nadkarni, J. D. Toussaint, Y. Yagi, B. E. Bouma, and G. J. Tearney, "Imaging the subcellular structure of human coronary atherosclerosis using micro-optical coherence tomography," *Nat. Med.* **17**(8), 1010–1014 (2011).
54. T. Bolmont, A. Bouwens, C. Pache, M. Dimitrov, C. Berclaz, M. Villiger, B. M. Wegenast-Braun, T. Lasser, and P. C. Fraering, "Label-free imaging of cerebral β -amyloidosis with extended-focus optical coherence microscopy," *J. Neurosci.* **32**(42), 14548–14556 (2012).
55. M. Yamanari, S. Nagase, S. Fukuda, K. Ishii, R. Tanaka, T. Yasui, T. Oshika, M. Miura, and Y. Yasuno, "Scleral birefringence as measured by polarization-sensitive optical coherence tomography and ocular biometric parameters of human eyes *in vivo*," *Biomed. Opt. Express* **5**(5), 1391–1402 (2014).
56. H. Wang, T. Akkin, C. Magnain, R. Wang, J. Dubb, W. J. Kostis, M. A. Yaseen, A. Cramer, S. Sakadžić, and D. Boas, "Polarization sensitive optical coherence microscopy for brain imaging," *Opt. Lett.* **41**(10), 2213–2216 (2016).
57. B. Baumann, A. Woehrer, G. Ricken, M. Augustin, C. Mitter, M. Pircher, G. G. Kovacs, and C. K. Hitzenberger, "Visualization of neuritic plaques in Alzheimer's disease by polarization-sensitive optical coherence microscopy," *Sci. Rep.* **7**(1), 43477 (2017).
58. M. Pircher, E. Götzinger, B. Baumann, and C. K. Hitzenberger, "Corneal birefringence compensation for polarization sensitive optical coherence tomography of the human retina," *J. Biomed. Opt.* **12**(4), 041210 (2007).
59. E. Götzinger, M. Pircher, I. Dejaco-Ruhswurm, S. Kaminski, C. Skorpik, and C. K. Hitzenberger, "Imaging of birefringent properties of keratoconus corneas by polarization-sensitive optical coherence tomography," *Invest. Ophthalmol. Visual Sci.* **48**(8), 3551–3558 (2007).
60. F. Beer, A. Wartak, R. Haindl, M. Gröschl, B. Baumann, M. Pircher, and C. K. Hitzenberger, "Conical scan pattern for enhanced visualization of the human cornea using polarization-sensitive OCT," *Biomed. Opt. Express* **8**(6), 2906–2923 (2017).
61. Y. Komai and T. Ushiki, "The three-dimensional organization of collagen fibrils in the human cornea and sclera," *Invest. Ophthalmol. Visual Sci.* **32**, 2244–2258 (1991).
62. W. Yuan, J. Mavadia-Shukla, J. Xi, W. Liang, X. Yu, S. Yu, and X. Li, "Optimal operational conditions for supercontinuum-based ultrahigh-resolution endoscopic OCT imaging," *Opt. Lett.* **41**(2), 250–253 (2016).
63. W. Drexler, U. Morgner, F. X. Kärtner, C. Pitris, S. A. Boppart, X. D. Li, E. P. Ippen, and J. G. Fujimoto, "*In vivo* ultrahigh-resolution optical coherence tomography," *Opt. Lett.* **24**(17), 1221–1223 (1999).
64. C. Canavesi and J. P. Rolland, "Ten years of Gabor-domain optical coherence microscopy," *Appl. Sci.* **9**(12), 2565 (2019).
65. F. A. South, Y.-Z. Liu, Y. Xu, N. D. Shemonski, P. S. Carney, and S. A. Boppart, "Polarization-sensitive interferometric synthetic aperture microscopy," *Appl. Phys. Lett.* **107**(21), 211106 (2015).
66. K. M. Meek, S. J. Tuft, Y. Huang, P. S. Gill, S. Hayes, R. H. Newton, and A. J. Bron, "Changes in collagen orientation and distribution in keratoconus corneas," *Invest. Ophthalmol. Visual Sci.* **46**(6), 1948–1956 (2005).
67. W. Lo, W.-L. Chen, C.-M. Hsueh, A. A. Ghazaryan, S.-J. Chen, D. H.-K. Ma, C.-Y. Dong, and H.-Y. Tan, "Fast Fourier transform-based analysis of second-harmonic generation image in keratoconic cornea," *Invest. Ophthalmol. Visual Sci.* **53**(7), 3501–3507 (2012).
68. N. Morishige, A. J. Wahlert, M. C. Kenney, D. J. Brown, K. Kawamoto, T. Chikama, T. Nishida, and J. V. Jester, "Second-harmonic imaging microscopy of normal human and keratoconus cornea," *Invest. Ophthalmol. Visual Sci.* **48**(3), 1087–1094 (2007).
69. N. Morishige, R. Shin-kyou-uchi, H. Azumi, H. Ohta, Y. Morita, N. Yamada, K. Kimura, A. Takahara, and K.-H. Sonoda, "Quantitative analysis of collagen lamellae in the normal and keratoconic human cornea by second harmonic generation imaging microscopy," *Invest. Ophthalmol. Visual Sci.* **55**(12), 8377–8385 (2014).